Sofia University "St. Kliment Ohridski"

Faculty of Physics

Tree Level Processes in Quantum Electrodynamics with a Dark Sector Extension

Elina Nestorova

Bachelor Thesis

Sofia, 2026

Abstract

This work presents a comprehensive calculation of differential cross section for the Møller scattering ($e^-e^- \to e^-e^-$) in quantum electrodynamics (QED). Beginning with defining of the QED Lagrangian from classical electrodynamics, we systematically develop the Feynman rules and compute the scattering amplitude using explicit momentum variables. The trace technology for gamma matrices is employed to evaluate squared matrix elements, yielding differential cross sections in the center-of-mass frame for each process. We present a comparison with the result from the computer event generator CalcHEP. Finally, we extend our treatement by the inclusion of a massive dark sector vector boson.

1. Introduction

In quantum electrodynamics (QED), the interactions between electrons, positrons, and photons are governed by a set of mathematical rules that arise from the Lagrangian of the theory. While the full theory is intricate, many essential features can be understood by studying the simplest processes, represented by *tree-level* Feynman diagrams. These diagrams correspond to the lowest-order contributions in a perturbative expansion and describe physical phenomena such as electron-electron (Møller) scattering, electron-positron (Bhabha) scattering, and photon-electron (Compton) scattering.

To appreciate how these diagrams emerge and what they mean, we begin with the Lagrangian of QED. This expression encapsulates both the free motion of electrons and photons, as well as their interactions.

The development of QED has been one of the central achievements in theoretical physics. Starting from Dirac's relativistic equation for the electron (1928), the theory naturally predicted the existence of antimatter, later confirmed experimentally with the discovery of the positron [1]. This breakthrough laid the foundation for a quantum field theoretical description of charged particles and their electromagnetic interactions.

Building upon Dirac's framework, the quantization of the electromagnetic field led to the modern formulation of QED. It was Feynman, together with Schwinger and Tomonaga, who in the 1940s developed the renormalized formulation of quantum electrodynamics and the tools required to compute observable quantities systematically [2–4]. Feynman's introduction of diagrammatic rules provided not only a practical computational method but also a powerful intuitive picture of how particles interact [4].

The importance of tree-level diagrams lies in their role as the starting point of perturbation theory. Although higher-order loop corrections are essential for achieving the remarkable precision of QED, tree-level processes capture the fundamental structure of particle interactions. They also provide the first approximation to experimental observables such as differential cross sections, which are directly measurable in scattering experiments.

Historically, electron scattering experiments have played a vital role in confirming the validity of QED. Measurements of angular distributions and total cross sections for Møller and Bhabha scattering provided some of the earliest quantitative tests of the theory. Even today, these processes serve as benchmarks in modern collider experiments, where they are used for detector calibration and luminosity measurements.

Thus, by studying tree-level diagrams in QED, we gain not only a computational foundation for more advanced processes but also an appreciation of the historical and experimental context that established QED as one of the most successful theories in physics.

Motivation from dark-photon searches

Beyond its role as a precision test of QED, lepton–lepton scattering is also an important tool in searches for physics beyond the Standard Model. One of the simplest extensions of QED is the dark-photon model, in which a new massive vector boson A' is introduced [5]. Its inclusion naturally relaxes the necessity of the quantization of the electric charge, which so far does not seem to be following from basic physical principles. The dark photon can interact weakly with ordinary charged particles through kinetic mixing with the Standard Model photon. This gives an effective coupling to electrons of the form

$$e_A = \varepsilon e,$$

where ε is the kinetic-mixing parameter. Comprehensive reviews of dark sectors and light weakly-coupled particles can be found in [6]. Because of this direct coupling to electrons, processes such as Møller scattering,

$$e^- e^- \to e^- e^-,$$

and Bhabha scattering,

$$e^+ e^- \to e^+ e^-,$$

are natural channels to study possible dark-photon effects.

Recent experimental and phenomenological work has placed particular emphasis on fixed-target experiments, where a high-intensity positron or electron beam scatters from atomic electrons in a thin target. In this context, Bhabha scattering plays a central role because it is both a Standard Model background and a normalization process for dark-sector searches. The PADME experiment at the Laboratori Nazionali di Frascati was designed to search for dark photons using the process

$$e^+ e^- \to \gamma A',$$

where the dark photon is reconstructed through the missing-mass technique [7, 8]. The same experimental environment also requires precise control of Standard Model reactions such as two-photon annihilation, bremsstrahlung, and radiative Bhabha scattering.

Recent PADME studies have therefore investigated not only the dark-photon signal itself, but also the relevant QED backgrounds. Measurements and simulations of annihilation and Bhabha-type processes are essential for understanding the detector response, estimating backgrounds, and extracting possible limits on the dark-photon parameter space [9]. In addition, PADME has been used to study scenarios connected with the proposed $X17$ boson, where resonant production in fixed-target positron–electron collisions can be tested [10]. Recent phenomenological work has also explored possible new-physics signatures in Bhabha scattering observables [11]. These developments show that ordinary QED scattering processes are not only textbook examples of perturbation theory, but also practical tools in modern searches for light hidden-sector particles.

For this reason, the present work first derives the tree-level QED result for Møller scattering in detail, using both analytic trace techniques and the event generator software CalcHEP. We then extend the same framework by replacing the massless photon propagator with a massive dark-photon propagator. This allows us to study how the differential cross section changes with the dark-photon coupling e_A and mass $m_{A'}$, and to connect the calculation with the broader phenomenology of dark-photon searches in lepton scattering.

2. From Classical Electrodynamics to Quantum Electrodynamics

Classical Foundations

In classical electrodynamics, the dynamics of the electromagnetic field are described by Maxwell's equations. These equations can be derived from a relativistically invariant Lagrangian density

$$\mathcal{L}_{\text{EM}} = -\frac{1}{4}F_{\mu\nu}F^{\mu\nu} - J^{\mu}A_{\mu}, \tag{1}$$

where A_μ is the electromagnetic four–potential and the field strength tensor is defined as

$$F_{\mu\nu} = \partial_\mu A_\nu - \partial_\nu A_\mu.$$

The first term describes the free electromagnetic field, while the second term represents the interaction between the electromagnetic field and a conserved four–current J^μ. Applying the Euler–Lagrange equations to this Lagrangian yields

$$\partial_\mu F^{\mu\nu} = J^\nu, \tag{2}$$

which correspond to the inhomogeneous Maxwell equations. The remaining Maxwell equations follow directly from the definition of the field strength tensor. Because $F_{\mu\nu}$ is constructed from derivatives of the potential, it satisfies the identity

$$\partial_\lambda F_{\mu\nu} + \partial_\mu F_{\nu\lambda} + \partial_\nu F_{\lambda\mu} = 0, \tag{3}$$

known as the *Bianchi identity*. When expressed in terms of the electric and magnetic fields, this identity leads to the homogeneous Maxwell equations

$$\nabla \cdot \mathbf{B} = 0, \qquad \nabla \times \mathbf{E} + \partial_t \mathbf{B} = 0.$$

The four–current J^μ is constrained by a conservation law that follows from *Noether's theorem*. If the Lagrangian is invariant under global phase transformations of the matter field,

$$\psi \to e^{i\alpha}\psi,$$

then a conserved current exists, satisfying

$$\partial_\mu J^\mu = 0. \tag{4}$$

This relation expresses the conservation of electric charge. Together with the Bianchi identity, it ensures that all four Maxwell equations emerge naturally from the electromagnetic Lagrangian. This provides the bridge from the compact relativistic formulation of electrodynamics to the familiar three–dimensional vector form used in classical physics.

Quantization and the Dirac Field

In quantum field theory, we promote classical fields to quantum operators. The current J^μ becomes an operator built from the Dirac field:

$$J^\mu \to \bar{\psi}\gamma^\mu\psi, \tag{5}$$

where ψ is the spinor field representing the electron, and $\bar{\psi} \equiv \psi^\dagger\gamma^0$ is its Dirac adjoint. The gamma matrices γ^μ satisfy the Clifford algebra:

$$\{\gamma^\mu, \gamma^\nu\} = 2g^{\mu\nu}. \tag{6}$$

The dynamics of a free spin-½ particle are governed by the Dirac Lagrangian:

$$\mathcal{L}_{\text{Dirac}} = \bar{\psi}(i\gamma^\mu\partial_\mu - m)\psi. \tag{7}$$

The QED Lagrangian

We can now combine the ingredients introduced above. The electromagnetic field is described by the Maxwell Lagrangian term $-\frac{1}{4}F_{\mu\nu}F^{\mu\nu}$, while the dynamics of the electron field are governed by the Dirac Lagrangian $\bar{\psi}(i\gamma^\mu\partial_\mu - m)\psi$. In quantum electrodynamics the classical current is replaced by the Dirac current introduced above, which couples the fermion field to the electromagnetic gauge field. Combining the free Dirac field, the electromagnetic field, and the interaction term yields the QED Lagrangian

$$\mathcal{L}_{\text{QED}} = \bar{\psi}(i\gamma^\mu\partial_\mu - m)\psi - \frac{1}{4}F_{\mu\nu}F^{\mu\nu} + e\bar{\psi}\gamma^\mu\psi A_\mu. \tag{8}$$

This compact expression contains three parts: the free electron field, the free electromagnetic field, and the interaction term describing the coupling between the electron current, and the photon field. From this Lagrangian the Feynman rules of QED can be systematically derived. The formulation of QED presented here follows standard treatments of quantum field theory and quantum electrodynamics [12, 13].

Gauge Symmetry

The group $U(1)$ consists of all complex phase rotations of unit magnitude, $e^{i\alpha}$, where α is a real parameter. In quantum field theory, such transformations correspond to changes in the overall phase of a charged field. A theory is said to have a global $U(1)$ symmetry if it is unchanged when the phase of all charged fields is rotated by the same constant amount everywhere in space and time. If the phase is allowed to vary from point to point ($\alpha \to \alpha(x)$), the symmetry becomes *local*, and requires the presence of a gauge field—in QED, this is the photon field A_μ—to preserve invariance. Local $U(1)$ invariance is therefore the fundamental gauge symmetry underlying QED.

Under a *global* $U(1)$ phase transformation with constant α,

$$\psi \;\to\; \psi' = e^{i\alpha}\psi, \quad \bar{\psi} \;\to\; \bar{\psi}' = \bar{\psi}e^{-i\alpha}, \quad A_\mu \;\to\; A_\mu,$$

the kinetic term transforms as

$$\bar{\psi}'\, i\gamma^\mu\partial_\mu\psi' = \bar{\psi}e^{-i\alpha}i\gamma^\mu\partial_\mu(e^{i\alpha}\psi) = \bar{\psi}i\gamma^\mu\partial_\mu\psi,$$

since α is constant. The mass term $-m\bar{\psi}\psi$ is trivially invariant, and the interaction term $e\,\bar{\psi}'\gamma^\mu\psi' A_\mu = e\,\bar{\psi}e^{-i\alpha}\gamma^\mu e^{i\alpha}\psi A_\mu = e\,\bar{\psi}\gamma^\mu\psi A_\mu$ is unchanged. The pure photon term $F_{\mu\nu}F^{\mu\nu}$ contains no ψ fields and is unaffected. Thus Eq. (8) is invariant under global $U(1)$ transformations.

For a *local* $U(1)$ transformation, α becomes a function of spacetime:

$$\psi \to e^{i\alpha(x)}\psi, \quad \bar{\psi} \to \bar{\psi} e^{-i\alpha(x)}, \quad A_\mu \to A_\mu - \frac{1}{e}\,\partial_\mu \alpha(x).$$

In this case, the derivative in the kinetic term produces an extra term proportional to $\partial_\mu \alpha(x)$ that is exactly canceled by the change in the interaction term when A_μ transforms as above. The field strength $F_{\mu\nu}$ is unchanged because the extra pieces cancel when antisymmetrized:

$$F'_{\mu\nu} = \partial_\mu A'_\nu - \partial_\nu A'_\mu = F_{\mu\nu}.$$

Therefore, Eq. (8) is invariant under local $U(1)$ gauge transformations, which is the defining symmetry of QED.

3. S-Matrix Expansion

In QED, the behavior of a system is determined by the *S-matrix*, which connects the initial and final quantum states of a process. This matrix is constructed from the time-ordered exponential of the interaction part of the Lagrangian:

$$S = \mathcal{T}\left\{\exp\left[-i \int d^4x\, \mathcal{H}_I(x)\right]\right\}, \tag{9}$$

where the interaction Hamiltonian density is

$$\mathcal{H}_I = -e\bar{\psi}\gamma^\mu \psi A_\mu. \tag{10}$$

To compute physical observables, the exponential is expanded into a Taylor series:

$$S = 1 - i\int d^4x\, \mathcal{H}_I(x) - \frac{1}{2}\int d^4x\, d^4y\, \mathcal{T}[\mathcal{H}_I(x)\mathcal{H}_I(y)] + \cdots \tag{11}$$

The lowest-order nontrivial terms in this expansion give rise to tree-level diagrams. Each term corresponds to a specific number of interaction vertices and thus a specific order in the coupling constant e.

From this expansion, one derives the so-called **Feynman diagrams**. Each diagram visually represents a term in the series and provides a recipe for computing the associated probability amplitude. External lines represent real particles entering or leaving the process, while internal lines (propagators) and vertices encode virtual particles and their interactions.

Importantly, the second-order term

$$\frac{1}{2}\int d^4x\, d^4y\, \mathcal{T}[\mathcal{H}_I(x)\mathcal{H}_I(y)]$$

leads directly to the fundamental **tree-level scattering processes** of QED, such as Møller scattering, Bhabha scattering, and Compton scattering.

4. Feynman Rules of QED and their Application to Møller Scattering

We are now going to look in detail at Moller Scattering. The perturbative expansion of the S-matrix leads naturally to a diagrammatic representation of scattering processes. Each diagram corresponds to a mathematical expression obtained by applying the Feynman rules of QED, which follow directly from the interaction term of the QED Lagrangian [12, 13].The Feynman rules emerge through path-integral quantization:

- The electron propagator is the Green's function of the Dirac equation.
- The photon propagator arises from inverting the wave operator in Maxwell's equations under gauge fixing.
- The interaction vertex follows directly from the QED interaction term $e\bar{\psi}\gamma^\mu\psi A_\mu$.
- External lines reflect the spinor solutions to the Dirac equation and photon polarization states.

In summary:

- each electron–photon vertex contributes a factor $(-ie)\gamma^\mu$,
- each internal photon line contributes a propagator $\dfrac{-ig_{\mu\nu}}{q^2}$,
- each internal electron line contributes a propagator $\dfrac{i(\not{p}+m)}{p^2-m^2+i\epsilon}$,
- each external electron line contributes a spinor $u(p)$ or $\bar{u}(p)$,
- each external photon line contributes a polarization vector $\epsilon_\mu(k)$.

With these rules, the diagrammatic approach reduces complicated time-ordered products to simple algebraic expressions. The diagrams not only serve as a visual shorthand but also enforce important physical principles such as conservation of momentum at each vertex and the proper symmetry (or antisymmetry) under exchange of identical particles.

Application to Møller scattering

At lowest order, $e^-e^- \to e^-e^-$ receives two contributions because the electrons are identical: a t-channel exchange and a u-channel exchange. The momentum labels are chosen so that p_1, p_2 are incoming and p_3, p_4 are outgoing, with the internal photon carrying

$$q_t = p_1 - p_3, \qquad q_u = p_1 - p_4.$$

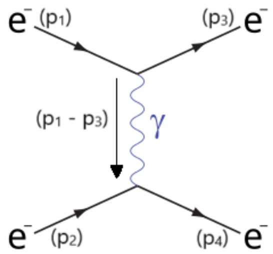

(a) t**-channel:** internal momentum $q_t = p_1 - p_3$, so $t = q_t^2$.

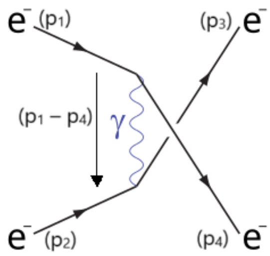

(b) u**-channel:** internal momentum $q_u = p_1 - p_4$, so $u = q_u^2$.

Figure 1: Tree-level Feynman diagrams for Møller scattering. Black (solid) lines are electrons with momenta p_i; the wavy line is the exchanged photon. The left diagram is the direct (t) channel; the right is the exchange (u) channel required by identical-fermion statistics.

From the diagrams to the matrix elements. Applying the QED Feynman rules:

- each electron–photon vertex contributes a factor $(-ie)\gamma^\mu$,
- the internal photon propagator gives $(-ig_{\mu\nu})/q^2$ with $q = q_t$ or q_u,
- external electron lines are represented by the spinors $\bar{u}(p_3), u(p_1), \bar{u}(p_4), u(p_2)$.

Throughout, we use the standard Mandelstam variables

$$s = (p_1 + p_2)^2, \qquad t = (p_1 - p_3)^2, \qquad u = (p_1 - p_4)^2, \tag{12}$$

which obey $s + t + u = \sum m_i^2 = 4m_e^2$ (and ≈ 0 in the ultrarelativistic limit $\sqrt{s} \gg m_e$).

Thus the two amplitudes are

$$\mathcal{M}_t = (-ie)^2 \frac{\left[\bar{u}(p_3)\gamma^\mu u(p_1)\right]\left[\bar{u}(p_4)\gamma_\mu u(p_2)\right]}{t}, \tag{13}$$

$$\mathcal{M}_u = (-ie)^2 \frac{\left[\bar{u}(p_4)\gamma^\mu u(p_1)\right]\left[\bar{u}(p_3)\gamma_\mu u(p_2)\right]}{u}. \tag{14}$$

Because the final-state electrons are indistinguishable, the total amplitude is the antisymmetrized combination

$$\mathcal{M} = \mathcal{M}_t - \mathcal{M}_u,$$

and the minus sign is the hallmark of Fermi statistics: exchanging two identical fermions introduces a relative minus sign.

Here and in the following we use the shorthand notation $u_i \equiv u(p_i)$ and $\bar{u}_i \equiv \bar{u}(p_i)$ for the Dirac spinors of the external electrons with momenta p_i.

It is convenient to collect the spinor bilinears into simpler objects. Starting from the total amplitude

$$\mathcal{M} = \mathcal{M}_t - \mathcal{M}_u = (-ie)^2 \left[\frac{\bar{u}_3 \gamma^\mu u_1 \, \bar{u}_4 \gamma_\mu u_2}{t} - \frac{\bar{u}_4 \gamma^\mu u_1 \, \bar{u}_3 \gamma_\mu u_2}{u} \right],$$

we define

$$A = \bar{u}_3 \gamma^\mu u_1, \qquad B = \bar{u}_4 \gamma_\mu u_2, \qquad C = \bar{u}_4 \gamma^\mu u_1, \qquad D = \bar{u}_3 \gamma_\mu u_2.$$

In terms of these objects, the amplitude takes the compact form

$$\mathcal{M} = -e^2 \left(\frac{AB}{t} - \frac{CD}{u} \right).$$

This notation will make the next steps (squaring the amplitude and performing the spin sums) much easier to follow.

In Fig. 1(a) the momentum flowing through the photon line is $q_t = p_1 - p_3$, so the denominator is $t = q_t^2$; in Fig. 1(b), $q_u = p_1 - p_4$ gives $u = q_u^2$. This is why, when we later compute $|\mathcal{M}|^2$, the squared amplitude will contain characteristic factors $1/t^2$, $1/u^2$, and an interference term $1/(tu)$.

5. Kinematics of Møller Scattering

In order to describe scattering processes quantitatively, we must understand how to assign momenta to the particles involved. We do this using **relativistic kinematics**, and it is particularly convenient to work in the *center-of-mass (COM)* frame — a reference frame in which the total spatial momentum of the system is zero. This simplifies calculations and has a direct physical interpretation: it is the frame where the colliding particles move directly toward each other with equal and opposite momenta.

Consider first a **generic** $2 \to 2$ **scattering process**. Let p_1 and p_2 denote the four-momenta of the incoming particles, and p_3 and p_4 those of the outgoing particles. In the COM frame, these momenta take the form:

$$
\begin{aligned}
p_1 &= (E, 0, 0, p), \\
p_2 &= (E, 0, 0, -p), \\
p_3 &= (E, p\sin\theta, 0, p\cos\theta), \\
p_4 &= (E, -p\sin\theta, 0, -p\cos\theta),
\end{aligned}
$$

where:

- E is the energy of each particle,
- $p = |\vec{p}|$ is the magnitude of the three-momentum,
- θ is the scattering angle — the angle between the incoming particle p_1 and the outgoing particle p_3.

This angle is what experiments measure when determining how far a particle is deflected after a collision.

The kinematic configuration can be visualized as follows:

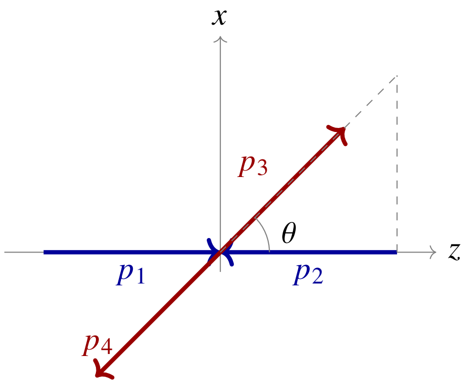

Fig. 1: Kinematics in the center-of-mass frame for a $2 \to 2$ scattering process. Blue arrows (p_1 and p_2) show the incoming particle momenta moving toward each other along the z-axis. Red arrows (p_3 and p_4) show the outgoing particle momenta, with θ the scattering angle of p_3 relative to the initial p_1 direction.

We now specialize this setup to the case of **Møller scattering**:

$$e^-(p_1) + e^-(p_2) \quad \longrightarrow \quad e^-(p_3) + e^-(p_4).$$

In our study, the incoming electrons each carry an energy

$$E = 0.55 \text{ GeV},$$

so that the total center-of-mass energy is

$$\sqrt{s} = 2E = 1.10\text{GeV}.$$

In the ultrarelativistic (massless) limit, the three-momentum magnitude satisfies $p \approx E$. Momentum conservation requires

$$p_1 + p_2 = p_3 + p_4,$$

and the scattering angle θ again denotes the deflection of the outgoing electron with momentum p_3 relative to the incoming beam direction of p_1.

Finally, we define the Mandelstam variables in this frame:

$$\begin{aligned} s &= (p_1 + p_2)^2 = 4E^2, \\ t &= (p_1 - p_3)^2 = -4E^2 \sin^2\left(\tfrac{\theta}{2}\right), \\ u &= (p_1 - p_4)^2 = -4E^2 \cos^2\left(\tfrac{\theta}{2}\right). \end{aligned}$$

These variables provide a compact way to express the scattering amplitude and will be directly used in the next section.

5.1 Physical picture and scattering channels in QED

The scattering angle θ provides physical insight into the interaction: forward scattering (small θ) corresponds to particles barely deflecting, while backward scattering (large θ) indicates strong exchange effects. The shape of the differential cross section as a function of θ reflects the underlying dynamics and the relative weight of different diagrams.

At tree level, each diagram corresponds to a different *channel*, classified by the Mandelstam variables:

- **s-channel:** annihilation followed by pair production (e.g. in Bhabha scattering).
- **t-channel:** scattering via exchange of a virtual photon; typically dominates forward scattering ($\theta \approx 0$).
- **u-channel:** exchange with final particles crossed; often dominates backward scattering ($\theta \approx \pi$).

In Møller scattering ($e^-e^- \to e^-e^-$), the electrons are identical, so both the t- and u-channel diagrams contribute and interfere.

6. Scattering Amplitude for Møller Scattering

We now proceed directly to the calculation of the spin-averaged squared amplitude.

The amplitudes for the t- and u-channel diagrams were derived in Section 4. The next step is to obtain measurable quantities, which requires squaring the total amplitude and averaging over the spins of the initial particles. This procedure naturally introduces traces of gamma matrices. Explicitly, the spin-averaged squared amplitude is

$$|\overline{\mathcal{M}}|^2 = \frac{1}{4}\sum_{\text{spins}} |\mathcal{M}|^2 = \frac{1}{4}\sum_{\text{spins}} \big(|\mathcal{M}_t|^2 + |\mathcal{M}_u|^2 + 2\mathrm{Re}(\mathcal{M}_t\mathcal{M}_u^*)\big).$$

The factor $1/4$ reflects the average over the 2×2 possible spin states of the two incoming electrons.

- $2\mathrm{Re}(\mathcal{M}_t\mathcal{M}_u^*)$ is the interference term between the two diagrams, which is essential because the final-state electrons are indistinguishable.

Let us now connect this general structure with the shorthand notation A, B, C, D introduced in the previous section. From

$$\mathcal{M} = -e^2\left(\frac{AB}{t} - \frac{CD}{u}\right)$$

we obtain, before spin averaging,

$$|\mathcal{M}|^2 = e^4\left(\frac{|AB|^2}{t^2} + \frac{|CD|^2}{u^2} - \frac{2\,\mathrm{Re}(AB\,(CD)^*)}{tu}\right).$$

The three pieces have a clear interpretation:

- $|AB|^2/t^2$ is the pure t-channel contribution,
- $|CD|^2/u^2$ is the pure u-channel contribution,
- the term with $2\,\mathrm{Re}(AB(CD)^*)$ is the interference between the two diagrams.

To perform the spin sums, we define

$$T = \sum_{\text{spins}} |AB|^2, \qquad U = \sum_{\text{spins}} |CD|^2, \qquad I = 2\sum_{\text{spins}} \mathrm{Re}(AB\,(CD)^*)\,,$$

so that

$$\sum_{\text{spins}} |\mathcal{M}|^2 = e^4\left(\frac{T}{t^2} + \frac{U}{u^2} - \frac{I}{tu}\right).$$

The rest of this section is devoted to computing T, U and I step by step using spin sums and trace identities.

To perform the spin sums we use the completeness relation

$$\sum_s u^{(s)}(p)\bar{u}^{(s)}(p) = \not{p} + m \quad \xrightarrow{m\to 0} \quad \not{p},$$

which converts bilinear spinor products into traces. For example, the t-channel contribution becomes

$$\sum_{\text{spins}} |\mathcal{M}_t|^2 = \frac{e^4}{t^2}\, \mathrm{Tr}\big[\not{p}_3\gamma^\mu\not{p}_1\gamma^\nu\big]\; \mathrm{Tr}\big[\not{p}_4\gamma_\mu\not{p}_2\gamma_\nu\big].$$

6.1 From amplitudes to traces

The measurable quantity is the squared amplitude averaged over initial spins:

$$|\overline{\mathcal{M}}|^2 = \frac{1}{4}\sum_{\text{spins}} |\mathcal{M}|^2 = \frac{1}{4}\sum_{\text{spins}} \big(|\mathcal{M}_t|^2 + |\mathcal{M}_u|^2 + 2\mathrm{Re}(\mathcal{M}_t\mathcal{M}_u^*)\big).$$

Here the spin sums convert bilinear spinor expressions such as

$$\bar{u}(p_3)\gamma^\mu u(p_1)\; \bar{u}(p_1)\gamma^\nu u(p_3)$$

into Dirac traces. In this notation: $u(p)$ is a free electron spinor of momentum p, $\bar{u}(p) \equiv u^\dagger(p)\gamma^0$ its Dirac adjoint, γ^μ are the Dirac gamma matrices obeying $\{\gamma^\mu, \gamma^\nu\} = 2g^{\mu\nu}$, and $\not{p} \equiv \gamma^\mu p_\mu$. All four-momenta p_1, p_2 (incoming) and p_3, p_4 (outgoing) are defined in the center-of-mass frame, with the Mandelstam invariants $s = (p_1 + p_2)^2$, $t = (p_1 - p_3)^2$, and $u = (p_1 - p_4)^2$.

To perform the spin sums explicitly, we use the completeness relation for Dirac spinors:

$$\sum_s u^{(s)}(p)\bar{u}^{(s)}(p) = \not{p} + m \quad \xrightarrow{m\to 0} \quad \not{p}.$$

This replacement turns products of bilinears into traces over gamma matrices, for example

$$\sum_{\text{spins}} \bar{u}(p_3)\gamma^\mu u(p_1)\; \bar{u}(p_1)\gamma^\nu u(p_3) \quad\longrightarrow\quad \mathrm{Tr}\left[\not{p}_3\gamma^\mu\not{p}_1\gamma^\nu\right].$$

Applying the completeness relations to the quantities T, U and I turns spinor products into traces over gamma matrices. Explicitly,

$$
\begin{aligned}
T &= \sum_{\text{spins}} |AB|^2 = \sum_{\text{spins}} \big(\bar{u}_3\gamma^\mu u_1\,\bar{u}_4\gamma_\mu u_2\big)\big(\bar{u}_1\gamma^\nu u_3\,\bar{u}_2\gamma_\nu u_4\big) \\
&= \mathrm{Tr}\big[\not{p}_3\gamma^\mu\not{p}_1\gamma^\nu\big]\ \mathrm{Tr}\big[\not{p}_4\gamma_\mu\not{p}_2\gamma_\nu\big]\,, && (15) \\
U &= \sum_{\text{spins}} |CD|^2 = \sum_{\text{spins}} \big(\bar{u}_4\gamma^\mu u_1\,\bar{u}_3\gamma_\mu u_2\big)\big(\bar{u}_1\gamma^\nu u_4\,\bar{u}_2\gamma_\nu u_3\big) \\
&= \mathrm{Tr}\big[\not{p}_4\gamma^\mu\not{p}_1\gamma^\nu\big]\ \mathrm{Tr}\big[\not{p}_3\gamma_\mu\not{p}_2\gamma_\nu\big]\,, && (16) \\
I &= 2\sum_{\text{spins}} \mathrm{Re}\big(AB\,(CD)^*\big) \\
&= -\,\mathrm{Tr}\big[\not{p}_3\gamma^\mu\not{p}_1\gamma^\nu\not{p}_4\gamma_\mu\not{p}_2\gamma_\nu\big]\,. && (17)
\end{aligned}
$$

We see explicitly that each factor AB or CD is replaced by a trace of four gamma matrices sandwiched between slashed momenta. In this way the problem of summing over spins is reduced to a purely algebraic problem involving traces and scalar products of four-momenta.

With this tool in hand, we can now evaluate the squared matrix elements for the t- and u-channel diagrams in Møller scattering. For example,

$$
\sum_{\text{spins}} |\mathcal{M}_t|^2 = \frac{e^4}{t^2}\,\mathrm{Tr}\big[\not{p}_3\gamma^\mu\not{p}_1\gamma^\nu\big]\ \mathrm{Tr}\big[\not{p}_4\gamma_\mu\not{p}_2\gamma_\nu\big].
$$

Similarly,

$$
\sum_{\text{spins}} |\mathcal{M}_u|^2 = \frac{e^4}{u^2}\,\mathrm{Tr}\big[\not{p}_4\gamma^\mu\not{p}_1\gamma^\nu\big]\ \mathrm{Tr}\big[\not{p}_3\gamma_\mu\not{p}_2\gamma_\nu\big], \tag{18}
$$

$$
2\,\mathrm{Re}(\mathcal{M}_t\mathcal{M}_u^*) = -\frac{2e^4}{tu}\,\mathrm{Tr}\big[\not{p}_3\gamma^\mu\not{p}_1\gamma^\nu\not{p}_4\gamma_\mu\not{p}_2\gamma_\nu\big]. \tag{19}
$$

This is the precise point where *traces over gamma matrices* enter the calculation, and the evaluation of these traces reduces the problem from spinor algebra to scalar products of momenta, which can then be written in terms of the Mandelstam invariants.

6.2 Trace identities

To evaluate the traces we use standard gamma-matrix identities [12]:

$$
\mathrm{Tr}[\gamma^\mu\gamma^\nu] = 4g^{\mu\nu}, \tag{20}
$$

$$
\mathrm{Tr}[\gamma^\mu\gamma^\nu\gamma^\rho\gamma^\sigma] = 4\big(g^{\mu\nu}g^{\rho\sigma} - g^{\mu\rho}g^{\nu\sigma} + g^{\mu\sigma}g^{\nu\rho}\big), \tag{21}
$$

$$
\mathrm{Tr}[\text{odd number of }\gamma^\mu] = 0 \tag{22}
$$

These reduce the traces to scalar products of four-momenta. For example,

$$\mathrm{Tr}[\not{a}\gamma^\mu \not{b}\gamma^\nu] = 4\big(a^\mu b^\nu + a^\nu b^\mu - g^{\mu\nu}(a\cdot b)\big).$$

As an explicit example, consider the first trace in T:

$$\mathrm{Tr}\big[\not{p}_3\gamma^\mu \not{p}_1\gamma^\nu\big] = 4\left(p_3^\mu p_1^\nu + p_3^\nu p_1^\mu - g^{\mu\nu}\, p_1\cdot p_3\right),$$

and similarly

$$\mathrm{Tr}\big[\not{p}_4\gamma_\mu \not{p}_2\gamma_\nu\big] = 4\left(p_{4\mu}p_{2\nu} + p_{4\nu}p_{2\mu} - g_{\mu\nu}\, p_2\cdot p_4\right).$$

Multiplying these two traces and contracting indices generates terms proportional to products of scalar products such as $(p_3\cdot p_4)(p_1\cdot p_2)$, $(p_3\cdot p_2)(p_1\cdot p_4)$ and $(p_3\cdot p_1)(p_2\cdot p_4)$.

All such scalar products can be expressed in terms of the Mandelstam variables. In the massless limit,

$$p_1\cdot p_2 = \frac{s}{2}, \qquad p_3\cdot p_4 = \frac{s}{2}, \tag{23}$$

$$p_1\cdot p_3 = -\frac{t}{2}, \qquad p_2\cdot p_4 = -\frac{t}{2}, \tag{24}$$

$$p_1\cdot p_4 = -\frac{u}{2}, \qquad p_2\cdot p_3 = -\frac{u}{2}, \tag{25}$$

with $s+t+u=0$. Substituting these relations and simplifying, one finds

$$T = \sum_{\text{spins}} |AB|^2 = 8\,(s^2+u^2), \qquad U = \sum_{\text{spins}} |CD|^2 = 8\,(s^2+t^2),$$

and

$$I = 2\sum_{\text{spins}} \mathrm{Re}(AB\,(CD)^*) = 16\,s^2.$$

Inserting these results back into

$$\sum_{\text{spins}} |\mathcal{M}|^2 = e^4\left(\frac{T}{t^2} + \frac{U}{u^2} - \frac{I}{tu}\right)$$

6.3 Result in terms of Mandelstam variables

Using these identities and expressing the dot products in terms of Mandelstam variables, we obtain

$$\sum_{\text{spins}} |\mathcal{M}_t|^2 = \frac{8e^4}{t^2}\left(s^2 + u^2\right), \tag{26}$$

$$\sum_{\text{spins}} |\mathcal{M}_u|^2 = \frac{8e^4}{u^2}\left(s^2 + t^2\right), \tag{27}$$

$$2\,\mathrm{Re}(\mathcal{M}_t \mathcal{M}_u^*) = \frac{16e^4}{tu}\, s^2. \tag{28}$$

The complete squared amplitude is therefore

$$|\overline{\mathcal{M}}|^2 = 2e^4 \left(\frac{s^2 + u^2}{t^2} + \frac{s^2 + t^2}{u^2} + \frac{2s^2}{tu} \right). \tag{29}$$

Finally, in the center-of-mass frame with ultrarelativistic electrons, the Mandelstam variables are

$$\begin{aligned} s &= 4E^2, \\ t &= -4E^2 \sin^2\left(\tfrac{\theta}{2}\right), \\ u &= -4E^2 \cos^2\left(\tfrac{\theta}{2}\right). \end{aligned}$$

Substituting these gives the angular form

$$\overline{|\mathcal{M}|^2} = 2e^4 \left(\frac{16E^4 + 16E^4 \cos^4\left(\frac{\theta}{2}\right)}{16E^4 \sin^4\left(\frac{\theta}{2}\right)} + \frac{16E^4 + 16E^4 \sin^4\left(\frac{\theta}{2}\right)}{16E^4 \cos^4\left(\frac{\theta}{2}\right)} + \frac{32E^4}{16E^4 \sin^2\left(\frac{\theta}{2}\right) \cos^2\left(\frac{\theta}{2}\right)} \right)$$

Simplifying:

$$\overline{|\mathcal{M}|^2} = 2e^4 \left(\frac{1 + \cos^4\left(\frac{\theta}{2}\right)}{\sin^4\left(\frac{\theta}{2}\right)} + \frac{1 + \sin^4\left(\frac{\theta}{2}\right)}{\cos^4\left(\frac{\theta}{2}\right)} + \frac{2}{\sin^2\left(\frac{\theta}{2}\right) \cos^2\left(\frac{\theta}{2}\right)} \right).$$

This explicit step-by-step derivation shows how the traces arise naturally from spin sums, and how they collapse to scalar products expressed in terms of the Mandelstam variables. The singular behavior for forward ($\theta \to 0$) and backward ($\theta \to \pi$) scattering is manifest.

7. Differential Cross Section and Comparison with CalcHEP

Having obtained the squared amplitude in the previous section, we now proceed to derive the analytic form of the differential cross section for Møller scattering in the center-of-mass frame.

From Squared Amplitude to Cross Section

The general relation between the squared amplitude and the differential cross section for a $2 \to 2$ process is

$$\frac{d\sigma}{d\Omega} = \frac{1}{128\pi^2 s} \, |\overline{\mathcal{M}}|^2,$$

where s is the Mandelstam invariant defined by $s = (p_1 + p_2)^2$.

In the high-energy limit, where the electron mass is negligible, the Mandelstam variables can be expressed directly in terms of the scattering angle θ in the center-of-mass frame:

$$s = 4E^2, \qquad t = -2E^2(1 - \cos\theta), \qquad u = -2E^2(1 + \cos\theta),$$

with E the energy of each incoming electron.

Substituting these expressions into the squared matrix element obtained in Sec. 6, the angular distribution of the cross section becomes

$$\frac{d\sigma}{d\cos\theta} = \frac{e^4}{16\pi s} \frac{(3 + z^2)^2}{(1 - z^2)^2}.$$

where we have introduced $z = \cos\theta$. This form makes explicit the characteristic singular behavior in the forward ($z \to +1$) and backward ($z \to -1$) directions.

Physical Interpretation

The dependence on the scattering angle carries important physical meaning. Forward scattering (small θ, i.e. $z \to 1$) corresponds to the electrons being only slightly deflected, while backward scattering (large θ, $z \to -1$) indicates strong exchange effects due to the indistinguishability of the two electrons. The divergence of the cross section in these limits is a well-known feature of QED processes with massless photon exchange.

8. Differential Cross Section and Comparison with CalcHEP

Having obtained the squared amplitude in the previous section, we now proceed to derive the analytic form of the differential cross section for Møller scattering in the center-of-mass frame.

From Squared Amplitude to Cross Section

The squared matrix element for Møller scattering, calculated via trace techniques and verified by the CalcHEP output, is

$$|\overline{\mathcal{M}}|^2 = 2e^4\left(\frac{s^2+u^2}{t^2} + \frac{s^2+t^2}{u^2} + \frac{2s^2}{tu}\right).$$

The general relation between the squared amplitude and the differential cross section for a $2 \to 2$ process is

$$\frac{d\sigma}{d\Omega} = \frac{1}{128\pi^2 s}\,|\overline{\mathcal{M}}|^2,$$

where $s = (p_1 + p_2)^2$.

In the high-energy limit, where the electron mass is negligible, the Mandelstam variables can be expressed directly in terms of the scattering angle θ in the center-of-mass frame:

$$s = 4E^2, \qquad t = -2E^2(1-\cos\theta) = -2E^2(1-z), \qquad u = -2E^2(1+\cos\theta) = -2E^2(1+z),$$

with E the energy of each incoming electron and $z = \cos\theta$.

Substituting these expressions into the squared matrix element and simplifying in *Mathematica* yields the compact form

$$\overline{|\mathcal{M}|^2} = 4e^4\,\frac{(3+z^2)^2}{(1-z^2)^2}.$$

The differential cross section then follows as

$$\frac{d\sigma}{d\cos\theta} = \frac{1}{2}\,\frac{1}{32\pi s}\,\overline{|\mathcal{M}|^2} = \frac{1}{64\pi s}\,\overline{|\mathcal{M}|^2} = \frac{e^4}{16\pi s}\,\frac{(3+z^2)^2}{(1-z^2)^2} = \frac{\pi\alpha^2}{s}\,\frac{(3+z^2)^2}{(1-z^2)^2},$$

where

$$\alpha \equiv \frac{e^2}{4\pi} \quad \text{(fine-structure constant in natural units } \hbar = c = 1\text{)}.$$

This expression exhibits sharp divergences as $z \to \pm 1$, corresponding to forward and backward scattering. These divergences are a hallmark of QED processes involving massless photon exchange and align perfectly with the shape observed in the CalcHEP-generated numerical graph.

Physical Interpretation

The dependence on the scattering angle carries important physical meaning. Forward scattering (small θ, i.e. $z \to 1$) corresponds to the electrons being only slightly deflected, while backward scattering (large θ, $z \to -1$) indicates strong exchange effects due to the indistinguishability of the two electrons. The divergence of the cross section in these limits is a well-known feature of

QED processes with massless photon exchange.

Comparison with CalcHEP

To verify the analytic derivation, we compare it with a numerical calculation performed in CalcHEP [14]. The software evaluates the same tree-level diagrams by applying Feynman rules automatically and outputs the differential cross section $d\sigma/d\cos\theta$.

The two results show complete qualitative agreement: both predict sharp rises in the forward ($\theta \to 0$) and backward ($\theta \to \pi$) regions, with a suppressed but nonzero cross section at intermediate angles. To make the comparison explicit, the analytic formula can be plotted alongside the CalcHEP output after appropriate normalization. The coincidence of the two curves demonstrates the consistency of our trace-based symbolic calculation with the automated numerical evaluation.

This cross-verification highlights how analytic and computational approaches complement each other: the former offers insight into the angular dependence and singular limits, while the latter provides efficient and precise numerical evaluation across the full kinematic range.

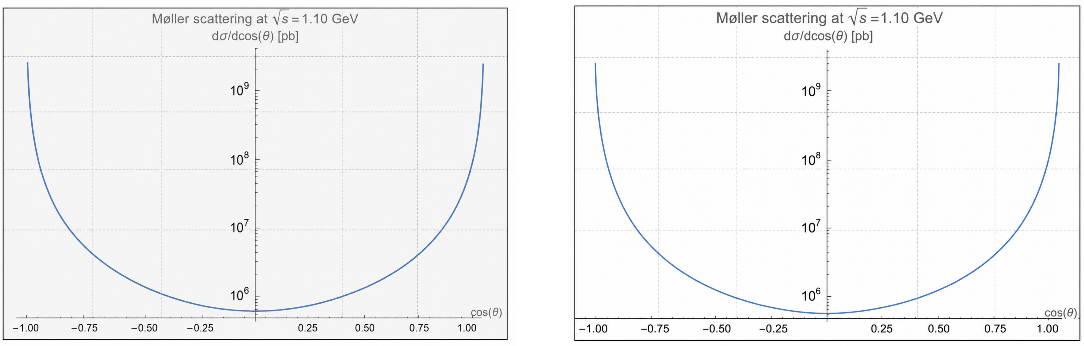

Figure 2: Comparison of the Møller-scattering differential cross section $d\sigma/d\cos\theta$ obtained numerically with CalcHEP (left) and analytically with Mathematica (right). Both results show strong forward and backward enhancements near $z = \pm 1$, as expected from the massless photon propagator.

Numerical Evaluation in CalcHEP

To verify the analytic result for the differential cross section, we use the event-generator package CalcHEP. This software automatically applies the Feynman rules of the Standard Model, generates the tree-level diagrams, and numerically evaluates the cross section as a function of the scattering angle.

Below we summarize the steps used to obtain the Møller–scattering distribution, together with screenshots of the program interface.

1. Entering the process. After launching CalcHEP, the main menu appears (Fig. 3). We select `Enter Process` and specify the process

$$e,\, e \;\longrightarrow\; e,\, e,$$

corresponding to Møller scattering.

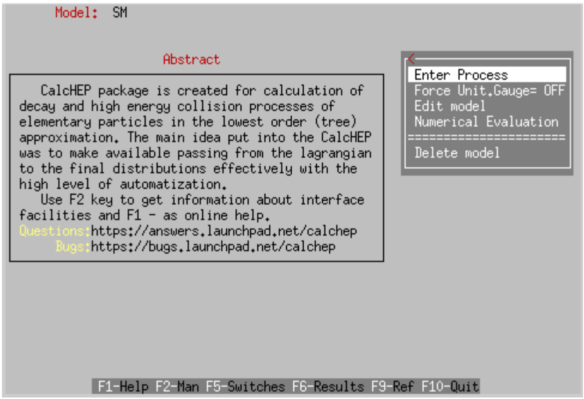

Figure 3: Main menu of CalcHEP.

2. Generating the Feynman diagrams. CalcHEP automatically constructs all tree-level diagrams consistent with the Standard Model Lagrangian. For Møller scattering, the program correctly produces the two expected diagrams: the t-channel photon exchange and the u-channel exchange (Fig. **??**). These follow directly from the antisymmetry of identical fermions.

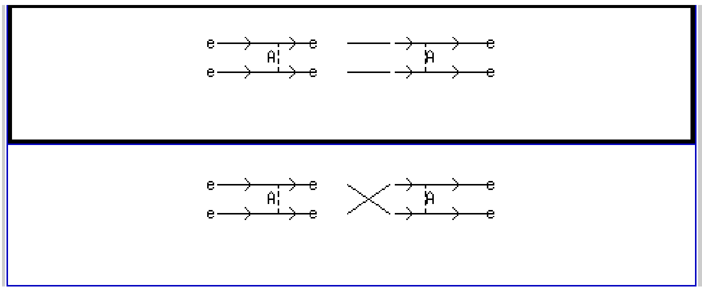

Figure 4: Tree-level Feynman diagrams for $e^-e^- \to e^-e^-$ generated by CalcHEP.

3. Creating the numerical session. After confirming the diagrams, we choose `Make and Launch` from the main menu, which opens the numerical evaluation module. Here we define the initial-state momenta. For the numerical evaluation, both incoming electrons are assigned an energy

$$E_1 = E_2 = 0.55 \text{ GeV},$$

corresponding to a center-of-mass energy

$$\sqrt{s} = 1.10 \text{ GeV}.$$

4. Accessing the differential cross section. Inside the numerical module we choose `1D integration`. This displays the total tree-level cross section for the process and allows us to compute angular distributions. Selecting `Angular dependence` and choosing a grid of 100 points in $\cos\theta$ instructs CalcHEP to evaluate the differential cross section $d\sigma/d\cos\theta$ numerically across the full angular range.

5. Result. The resulting curve shows the characteristic sharp rise as $\cos\theta \to \pm 1$, corresponding to forward and backward scattering. This behaviour originates from the massless photon propagator, which produces the familiar $1/t^2$ and $1/u^2$ singularities in the analytic expression. The shape agrees precisely with the analytic formula derived in the previous section:

$$\frac{d\sigma}{d\cos\theta} = \frac{\pi\alpha^2}{s}\frac{(3+z^2)^2}{(1-z^2)^2}, \qquad z = \cos\theta.$$

To visualize the angular dependence of the cross section, the analytic expression for $d\sigma/d\cos\theta$ was evaluated numerically in Mathematica and plotted as a function of

$$z = \cos\theta.$$

Because the cross section diverges strongly in the forward and backward directions ($z \to \pm 1$), the vertical axis is displayed on a logarithmic scale. This makes the full angular behaviour visible, including the sharp peaks near $z = \pm 1$ produced by the $1/t^2$ and $1/u^2$ photon propagators.

Thus CalcHEP confirms the full angular dependence predicted by QED.

9. Dark photon model setup

In this chapter we repeat the entire Møller–scattering analysis from the previous sections, but now replacing the massless photon by a light dark photon. We keep the same kinematic conditions as before, with both incoming electrons carrying an energy of 0.55 GeV, same scattering geometry, same Mandelstam definitions), and we only modify the interaction by introducing a new mediator. The dark-photon model was implemented in LanHEP [15]. After defining the model, we generate the diagrams and the squared matrix element in CalcHEP, extract the analytic expression into Mathematica, and compute the differential cross section $\mathrm{d}\sigma/\mathrm{d}\cos\theta$ step by step, and finally compare the analytic formula to the numerical output in order to see how the dark photon changes the behaviour of Møller scattering.

The model used for this purpose is:

```
model QED_Moller_DP/1.
```

```
parameter ee1 = 0.000303: 'Rescaled electric charge (eps * e)'.

vector A1/A1: (gauge, mass MA = 0.017).

spinor e1: (electron, mass me = 0.000511).

lterm ee1*E1*gamma*A1*e1.
```

model QED_Moller_DP/1. Declares the name and version of the dark-photon extension of the QED Møller model.

parameter ee1 = 0.000303. Defines the effective dark-photon coupling $e' = \varepsilon e$, chosen to be about 10^{-3} of the usual electric charge.

vector A1/A1: (gauge, mass MA = 0.017). Introduces the dark photon A'_μ as a massive gauge boson with mass $M_A = 0.017$ GeV.

spinor e1: (electron, mass me = 0.000511). Declares the electron field with its physical mass for use in the numerical computations.

lterm ee1*E1*gamma*A1*e1. Adds the interaction term $e'\,\bar{e}\gamma^\mu e\,A'_\mu$, generating the electron–dark-photon vertex in the Feynman rules.

9.1 Generation of the dark–photon Møller diagrams in CalcHEP

After importing the model `QED_Moller_DP/1` into CalcHEP, we define the scattering process

$$e1,\ e1\ \rightarrow\ e1,\ e1$$

exactly as in the pure QED case. The only difference is that the mediator is now the massive dark photon A1. CalcHEP automatically constructs all tree–level diagrams that follow from the interaction term `lterm ee1*E1*gamma*A1*e1`.

Figure 5 shows the resulting diagrams. They have the same structure as the familiar QED Møller graphs, but with the photon propagator replaced by a dark-photon propagator.

The two diagrams correspond to the two possible ways of connecting the incoming and outgoing identical electrons:

- a *t-channel* exchange, where momentum flows as $q = p_1 - p_3$,
- a *u-channel* exchange, with momentum $q = p_1 - p_4$.

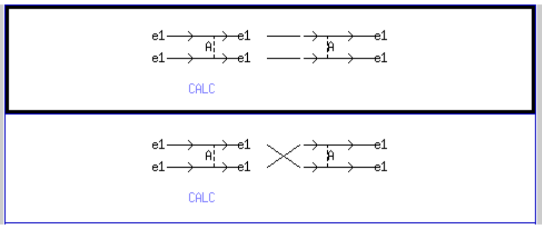

Figure 5: Tree–level diagrams for dark–photon–mediated Møller scattering. The dark photon A1 is exchanged in the t-channel and u-channel.

Because the electrons are identical particles, both diagrams must be included and they interfere with each other.

9.2 Extracting the squared matrix element from CalcHEP

CalcHEP can output the symbolic expression for the full spin–summed $|\mathcal{M}|^2$ in a Mathematica–readable form. When we select `Symbolic Calculation`, CalcHEP produces two expressions: one for each diagram, including the interference terms.

The result, once loaded into Mathematica, appears as:

```
p4 = +p1+p2-p3;
p1/: SC[p1,p1] = me^2;
p2/: SC[p2,p2] = me^2;
p3/: SC[p3,p3] = me^2;
p2/: SC[p2,p3] = -1*(me^2-me^2-me^2-me^2-2*SC[p1,p2]
                    +2*SC[p1,p3])/2;

initSum;

(* Diagram 1 *)
totFactor = ((8*eA^4)/(1));
numerator =(SC[p1,p3]^2 - 2*SC[p1,p3]*SC[p1,p2]
            - 4*SC[p1,p3]*me^2 + 2*SC[p1,p2]^2
            + 2*SC[p1,p2]*me^2 + 3*me^4);
denominator =(propDen[-p1+p3,mA,0]^2);

addToSum;

(* Diagram 2 *)
totFactor = ((8*eA^4)/(1));
numerator =(SC[p1,p2]^2 - 2*SC[p1,p2]*me^2);
denominator =(propDen[-p1+p3,mA,0] * propDen[-p1+p4,mA,0]);
```

```
addToSum;

finishSum;
```

CalcHEP expresses the matrix element in terms of the scalar products $\mathrm{SC}[p_i, p_j] = p_i \cdot p_j$ and the propagator function `propDen`. The instruction `initSum` starts the construction of the full $|\mathcal{M}|^2$, and `finishSum` prints the final expression.

To interpret this output, we note:

- $\mathrm{propDen}[-p_1 + p_3, m_A, 0] = t - m_A^2$,
- $\mathrm{propDen}[-p_1 + p_4, m_A, 0] = u - m_A^2$,
- the numerators correspond to the spin traces of the two diagrams.

Thus the CalcHEP result is exactly the analytic dark–photon amplitude.

9.3 Simplifying the amplitude in Mathematica

We now simplify the CalcHEP expression in Mathematica by:

1. substituting the Mandelstam relations $s = (p_1 + p_2)^2,\ t = (p_1 - p_3)^2,\ u = (p_1 - p_4)^2$,
2. replacing the scalar products with $SC[p_1, p_2] = \frac{s}{2},\ SC[p_1, p_3] = -\frac{t}{2}$, in the massless limit,
3. rewriting the propagators as $(t - m_A^2)^{-1},\ (u - m_A^2)^{-1}$,
4. symmetrizing the result under $t \leftrightarrow u$.

After these steps, Mathematica produces a compact form of the squared matrix element,

$$\overline{|\mathcal{M}|^2}(s, \theta) = \frac{4e_A^4 s^2}{\big(2m_A^2 + s(1 - \cos\theta)\big)^2 \big(2m_A^2 + s(1 + \cos\theta)\big)^2}\, \mathcal{N}(s, \cos\theta, m_A),$$

where $\mathcal{N}$ is the polynomial in s, m_A, and $\cos\theta$ that we derive analytically in the next subsection.

To get the differential cross section in Mathematica, we insert $\overline{|\mathcal{M}|^2}$ into the standard $2 \to 2$ formula,

$$\frac{d\sigma}{d\cos\theta} = \frac{1}{64\pi s}\, \overline{|\mathcal{M}|^2}\big(s, t(\theta), u(\theta)\big),$$

with

$$t(\theta) = -\frac{s}{2}(1 - \cos\theta), \qquad u(\theta) = -\frac{s}{2}(1 + \cos\theta).$$

The resulting differential cross section is shown in Figure 6 The behaviour is qualitatively similar to QED Møller scattering, but the massive dark photon regulates the forward and backward divergences and changes the overall normalisation through the rescaled coupling e_A.

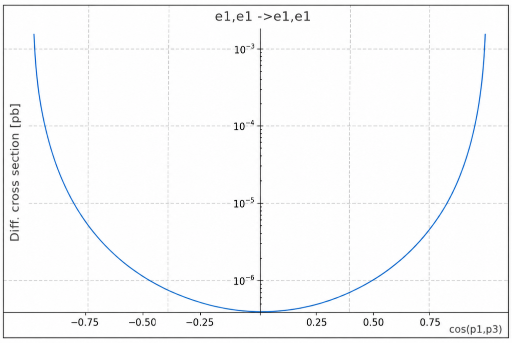

Figure 6: Differential cross section for dark–photon–mediated Møller scattering from CalcHEP, shown as a function of $\cos\theta$.

Next, we plot the differential cross section in Mathematica.

The resulting distribution is shown in the figure below. The curve is symmetric under $z \to -z$, as expected for Møller scattering of identical electrons.

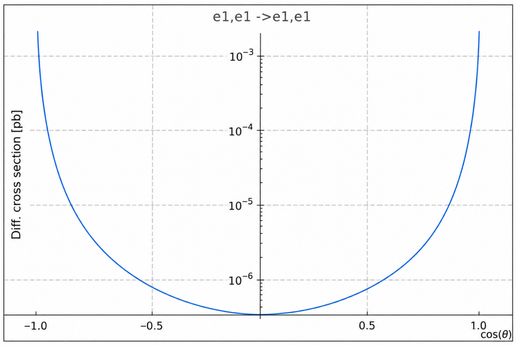

Figure 7: Differential cross section for dark–photon–mediated Møller scattering from Wolfram Mathematica, shown as a function of $\cos\theta$.

As in the ordinary QED case, the cross section increases toward the forward and backward directions. However, because the exchanged boson is now massive, the propagator denominators are

$$t - m_{A'}^2, \qquad u - m_{A'}^2,$$

instead of t and u. This softens the sharp divergences of the massless-photon case and leads to a smoother angular behaviour near $\cos\theta = \pm 1$.

The overall normalization is also strongly reduced, since the dark-photon coupling e_A is much smaller than the ordinary QED coupling. Thus the Mathematica plot makes the physical effect of the dark photon immediately visible: compared with Standard Model Møller scattering, the angular distribution remains peaked in the forward and backward regions, but the peaks are regulated by the mediator mass and suppressed by the weaker coupling.

9.4 Dependence on the Dark-Photon Interaction Constant

In this subsection, we investigate how the differential cross section changes when the strength of the dark-photon interaction is varied. This allows us to isolate the role of the coupling constant in the scattering process.

Physical idea. In the dark-photon model, the interaction between the electron and the mediator is controlled by the effective coupling

$$e_A = \epsilon e.$$

Since the squared matrix element is proportional to the fourth power of the coupling,

$$|\mathcal{M}|^2 \propto e_A^4,$$

the differential cross section inherits the same dependence:

$$\frac{d\sigma}{d\cos\theta} \propto e_A^4.$$

This means that even a small change in the coupling leads to a very large change in the overall magnitude of the cross section.

Setup of the calculation. We keep the kinematics and mediator mass fixed, using the same parameters as in the previous subsection:

$$\sqrt{s} = 1.10 \text{ GeV}, \qquad m_A = 0.017 \text{ GeV}.$$

The Mandelstam variables in the center-of-mass frame are expressed in terms of

$$z = \cos\theta$$

as

$$t(z) = -\frac{s}{2}(1-z), \qquad u(z) = -\frac{s}{2}(1+z).$$

For the dark-photon exchange, the propagators are modified according to

$$t \to t - m_A^2, \qquad u \to u - m_A^2.$$

Substituting these into the squared matrix element, the differential cross section becomes

$$\frac{d\sigma}{d\cos\theta} = \frac{1}{64\pi s} \cdot 2e_A^4 \left[\frac{s^2+u^2}{(t-m_A^2)^2} + \frac{s^2+t^2}{(u-m_A^2)^2} + \frac{2s^2}{(t-m_A^2)(u-m_A^2)} \right].$$

Numerical evaluation. To visualize the dependence on the coupling, we evaluate the above expression numerically in *Mathematica* for three different values:

$$e_A = 10^{-4}, \qquad e_A = 10^{-5}, \qquad e_A = 10^{-6}.$$

The result is plotted as a function of $z = \cos\theta$ over the interval

$$-0.99 \leq z \leq 0.99,$$

excluding the endpoints where the cross section becomes large.

A logarithmic scale is used for the vertical axis in order to clearly display the large differences in magnitude between the curves.

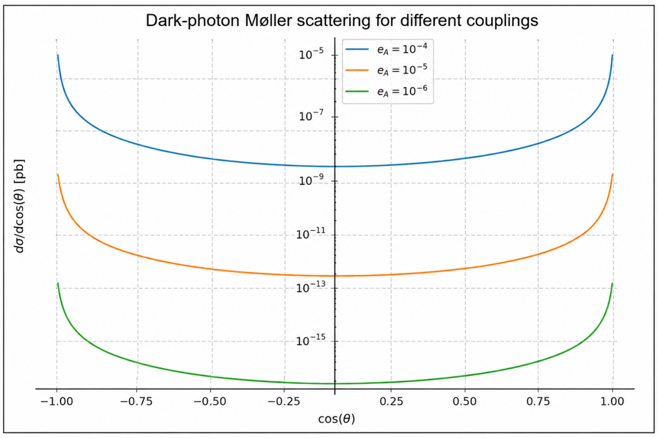

Figure 8: Differential cross section for dark-photon-mediated Møller scattering for three different interaction constants $e_A = 10^{-4}, 10^{-5}, 10^{-6}$, with fixed mediator mass $m_A = 0.017$ GeV and center-of-mass energy $\sqrt{s} = 1.10$ GeV.

Discussion of the result. The three curves exhibit identical angular dependence, confirming that the shape of the distribution is determined primarily by the kinematics and the propagator structure.

The only difference between the curves is their overall normalization. As the coupling decreases, the entire distribution is uniformly suppressed. This behavior is a direct consequence of the proportionality

$$\frac{d\sigma}{d\cos\theta} \propto e_A^4.$$

In particular, decreasing the coupling by one order of magnitude reduces the cross section by four orders of magnitude. This demonstrates that the dark-photon contribution becomes rapidly negligible for small couplings.

The analysis shows that the interaction constant controls the overall strength of the scattering process, while the angular dependence remains unchanged.

9.5 Dependence on the Dark-Photon Mass

We now study how the differential cross section changes when the mass of the dark photon is varied, while keeping the interaction strength fixed. This allows us to isolate the effect of the mediator mass on the scattering process.

Physical idea. In contrast to the interaction constant, which only affects the overall normalization of the cross section, the mass of the mediator enters directly into the propagators:

$$t \longrightarrow t - m_A^2, \qquad u \longrightarrow u - m_A^2.$$

This means that the mass modifies the *angular dependence* of the cross section. In particular, a nonzero mass regulates the divergences that appear in the forward and backward directions in the massless case.

Setup of the calculation. We keep the coupling constant fixed at

$$e_A = 10^{-4},$$

and use the same center-of-mass energy as before:

$$\sqrt{s} = 1.10 \text{ GeV}.$$

We now consider three different values of the dark-photon mass:

$$m_A = 0.001 \text{ GeV}, \qquad m_A = 0.01 \text{ GeV}, \qquad m_A = 0.1 \text{ GeV}.$$

The Mandelstam variables are expressed in terms of

$$z = \cos\theta$$

as

$$t(z) = -\frac{s}{2}(1-z), \qquad u(z) = -\frac{s}{2}(1+z).$$

The differential cross section is given by

$$\frac{d\sigma}{d\cos\theta} = \frac{1}{64\pi s} \cdot 2e_A^4 \left[\frac{s^2+u^2}{(t-m_A^2)^2} + \frac{s^2+t^2}{(u-m_A^2)^2} + \frac{2s^2}{(t-m_A^2)(u-m_A^2)} \right].$$

Numerical evaluation. The expression is evaluated numerically in *Mathematica* for the three mass values listed above, keeping the coupling fixed.

The result is plotted as a function of $z = \cos\theta$ in the interval

$$-0.99 \le z \le 0.99,$$

again avoiding the endpoints where the cross section becomes large.

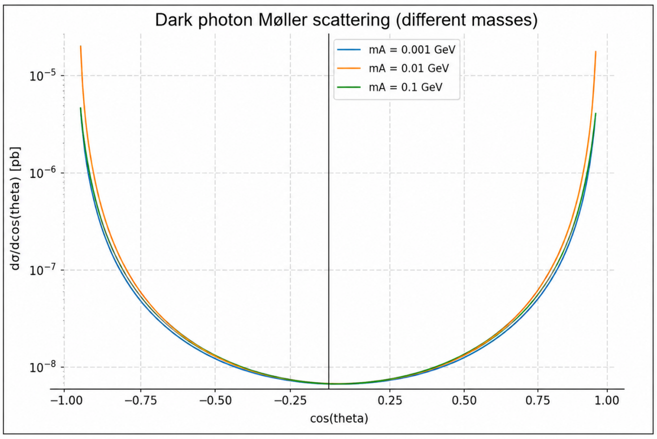

Figure 9: Differential cross section $d\sigma/d\cos\theta$ for dark-photon-mediated Møller scattering for three different mediator masses m_A, with fixed coupling $e_A = 10^{-4}$.

In Fig. 9, the curve for the smallest mass, $m_A = 0.001$ GeV, is not clearly visible because it almost completely overlaps with the curve for $m_A = 0.01$ GeV. For these small masses, the term m_A^2 in the propagator denominators,

$$t - m_A^2, \qquad u - m_A^2,$$

is much smaller than the typical values of the kinematic variables t and u over most of the angular range. Therefore, changing the mass from 0.001 GeV to 0.01 GeV produces only a very small change in the differential cross section.

As a result, the corresponding curves lie almost on top of each other on the logarithmic plot. The blue curve is therefore hidden behind the other curve rather than absent. This shows that, for sufficiently light dark photons, the angular distribution is nearly insensitive to the exact value of m_A.

Discussion of the result. Unlike the case of varying the coupling, the three curves now differ not only in magnitude but also in shape.

For the smallest mass, $m_A = 0.001$ GeV, the behavior closely resembles the massless photon case: the cross section exhibits sharp peaks in the forward and backward directions. This is because the propagators are dominated by the kinematic variables t and u.

As the mass increases, the denominators

$$t - m_A^2, \qquad u - m_A^2$$

no longer approach zero as rapidly. This softens the singular behavior and reduces the height of the peaks near $z = \pm 1$.

For the largest mass, $m_A = 0.1$ GeV, the angular distribution becomes significantly smoother, and the forward/backward enhancement is strongly suppressed.

10. Conclusion

In this work, we studied tree-level scattering processes in quantum electrodynamics with a particular focus on Møller scattering. Starting from the classical electromagnetic Lagrangian, we introduced the quantization procedure leading to the QED Lagrangian and the corresponding Feynman rules. Using these rules, the scattering amplitudes for the t- and u-channel diagrams were derived explicitly, and the spin-averaged squared matrix element was calculated step by step through the use of gamma-matrix trace techniques and Mandelstam variables.

The analytic derivation of the differential cross section demonstrated the characteristic angular behaviour of QED scattering processes mediated by a massless photon. In particular, strong forward and backward enhancements appear due to the $1/t^2$ and $1/u^2$ dependence of the photon propagators. The resulting analytic expression was then compared with numerical calculations performed in CalcHEP, showing complete qualitative agreement between the symbolic derivation and the automated computational approach.

The second part of the work extended the Standard Model interaction by introducing a massive dark photon. After implementing the model in LanHEP and generating the corresponding amplitudes in CalcHEP, the differential cross section for dark-photon-mediated Møller scattering was derived and analyzed numerically in Mathematica. Unlike the ordinary QED case, the presence of a nonzero mediator mass modifies the propagator structure and regulates the strong singular behaviour in the forward and backward directions.

The dependence of the differential cross section on the dark-photon coupling constant and mediator mass was investigated in detail. Varying the interaction strength showed that the coupling primarily changes the overall normalization of the cross section, consistent with the proportionality

$$\frac{d\sigma}{d\cos\theta} \propto e_A^4.$$

In contrast, varying the mediator mass changed the shape of the angular distribution itself, demonstrating how a massive propagator softens the characteristic QED enhancement near $\cos\theta = \pm 1$.

The results obtained in this work illustrate both the predictive power of perturbative quantum field theory and the usefulness of computational tools such as CalcHEP, LanHEP, and Mathematica for modern particle-physics calculations. At the same time, they show how well-known QED scattering processes can be extended naturally to explore possible physics beyond the Standard

Model. In particular, dark-photon searches in fixed-target experiments such as PADME provide an important phenomenological motivation for studying modified lepton-scattering processes and their angular distributions.

Overall, the work demonstrates how analytic calculations, numerical simulations, and phenomenological extensions beyond the Standard Model can be combined within a unified framework to study fundamental particle interactions.

References

[1] Paul A. M. Dirac. The quantum theory of the electron. *Proc. Roy. Soc. Lond. A*, 117:610–624, 1928.

[2] Julian Schwinger. On quantum-electrodynamics and the magnetic moment of the electron. *Physical Review*, 73:416–417, 1948.

[3] S. Tomonaga. On a relativistically invariant formulation of the quantum theory of wave fields. *Prog. Theor. Phys.*, 1:27–42, 1946.

[4] R. P. Feynman. Space - time approach to quantum electrodynamics. *Phys. Rev.*, 76:769–789, 1949.

[5] Bob Holdom. Two U(1)'s and Epsilon Charge Shifts. *Phys. Lett. B*, 166:196–198, 1986.

[6] Rouven Essig et al. Working Group Report: New Light Weakly Coupled Particles. In *Snowmass 2013: Snowmass on the Mississippi*, 10 2013.

[7] Mauro Raggi, Venelin Kozhuharov, and P. Valente. The PADME experiment at LNF. *EPJ Web Conf.*, 96:01025, 2015.

[8] Andre Frankenthal. Searching for Dark Photons with PADME. In *Meeting of the Division of Particles and Fields of the American Physical Society*, 10 2019.

[9] F. Bossi et al. Cross-section measurement of two-photon in-flight annihilation of positrons at s=20 MeV with the PADME detector. *Phys. Rev. D*, 107(1):012008, 2023.

[10] Luc Darmé, Marco Mancini, Enrico Nardi, and Mauro Raggi. Resonant search for the X17 boson at PADME. *Phys. Rev. D*, 106(11):115036, 2022.

[11] Aleksandr Pustyntsev, Muthubharathi S. Ramasamy, and Marc Vanderhaeghen. New physics searches via beam normal spin asymmetry in Bhabha scattering. *Phys. Rev. D*, 113(7):075032, 2026.

[12] Michael E. Peskin and Daniel V. Schroeder. *An Introduction to quantum field theory*. Addison-Wesley, Reading, USA, 1995.

[13] Matthew D. Schwartz. *Quantum Field Theory and the Standard Model*. Cambridge University Press, 3 2014.

[14] Alexander Belyaev, Neil D. Christensen, and Alexander Pukhov. CalcHEP 3.4 for collider physics within and beyond the Standard Model. *Comput. Phys. Commun.*, 184:1729–1769, 2013.

[15] A. Semenov. LanHEP: A Package for the automatic generation of Feynman rules in field theory. Version 3.0. *Comput. Phys. Commun.*, 180:431–454, 2009.